Downloaded from UvA-DARE, the institutional repository of the University of Amsterdam (UvA)
http://dare.uva.nl/document/122469

File ID	122469
Filename	6: Matter-wave interference
Version	Final published version (publisher's pdf)

SOURCE (OR PART OF THE FOLLOWING SOURCE):

Type	Dissertation
Title	Bose-Einstein condensates in radio-frequency-dressed potentials on an atom chip
Author	J.J.P. van Es
Faculty	Faculty of Science
Year	2009
Pages	VIII, 131
ISBN	978-90-5776-186-7

FULL BIBLIOGRAPHIC DETAILS:
http://dare.uva.nl/record/292198

Copyright

It is not permitted to download or to forward/distribute the text or part of it without the consent of the author(s) and/or copyright holder(s), other then for strictly personal, individual use.

UvA-DARE is a service provided by the library of the University of Amsterdam (http://dare.uva.nl)

6 Matter-wave interference

6.1 Introduction

Matter-wave interference is at the heart of quantum mechanics [167, 168], and is also of practical importance in the form of e.g. electron diffraction [169], electron microscopy [170, 171] and neutron interferometry [172]. Interferometry based on free neutral *atoms* has also already been used for high-precision measurements of a number of physical quantities [173]. Much more recently, it became possible to employ samples of ultra cold *trapped* atoms to generate matter-wave interference and study the properties of these quantum systems [72, 79, 82, 174].

The experiments detailed in this chapter provide the basis for on-going experiments aimed at investigating interference between degenerate Bose gases in and near the one-dimensional regime. For this purpose we discuss the optimization performed in order to observe clear interference patterns between condensates split using the rf-dressed double-well potential. Emphasis is then given to two key properties of the interference signal: the phase stability over time and the phase distribution along the length of the interfering clouds. For vertically-split condensates we observe curved, or even wiggled, interference fringes characteristic of phase fluctuations in one-dimensional quasi-condensates.

This chapter is organized as follows. In Sec. 6.2 we provide background information related to atom interferometers in general and some issues that are specific to interferometers employing ultra-cold trapped atoms. These issues include the development of the interference pattern in expanding condensates, the peculiar character of the phase coherence in elongated condensates and the characteristic shape of the double-well potential used to split a single BEC. In Sec. 6.3 we discuss the general experimental procedure for the experiments presented in this chapter. We then continue by describing two experiments aimed at optimizing experimental conditions for observing matter-wave interference. In the first we vary the hold time in the bare potential after switch-off of the rf-dressing field to further characterize the potential. The second experiment is aimed at optimization of the switch-off procedure of the rf-dressed potential. Section 6.4 describes the interference experiment. We release two condensates from a vertically-split double-well potential to expand and overlap them in time-of-flight, revealing an interference pattern. We provide a detailed analysis of the interference pattern to determine contrast and phase. The splitting is partially phase coherent. We observe the evolution of the condensate phase differ-

ence in the double-well. We analyze spatial fluctuations of the phase to determine the relative phase coherence length. We conclude this chapter with a summary of the results and an outlook on future interference experiments.

6.2 Background information

6.2.1 Interfering atoms

Before discussing interference of trapped clouds of quantum-degenerate ultra-cold atoms, we first give some background on more conventional atom interferometers, in which beams of neutral atoms are split and recombined to yield an interference pattern [173, 175]. Atom interferometers fit in the broader picture of atom optics in which the trajectories and the wave properties of neutral atoms are manipulated similar to the manipulation of light in optics [176]. In atom interferometers the wavelength of relevance is the de Broglie wavelength

$$\lambda_{\mathrm{dB}} = \frac{h}{Mv}, \tag{6.1}$$

where h is Planck's constant, M the atomic mass and v the velocity of the atom. Compared to light interferometers that have a long tradition of precision measurements, atom interferometers are relatively new. The idea was patented in 1973 [177], but the first atom interferometers only appeared in 1991 [178–181]. Development of working devices was hindered by the lack of suitable beamsplitters and by the achievable de Broglie wavelength which is generally much shorter than the wavelength of visible light. Beamsplitters are made of nanostructured gratings or standing-wave light beams. The reason why considerable effort was put in the development of these interferometers is the prospect of a very high precision. In a realistic scenario potential differences of 6.6×10^{-12} eV in a 10 cm interaction region should be measurable (see [173]). Also the atom interferometer has advantages with respect to devices that operate on neutrons or electrons. A beam of atoms is much easier to obtain than a beam of neutrons for which an accelerator or nuclear reactor is needed. The lack of net charge makes atoms robust against stray fields when compared to electrons. By now atom interferometers have been used to sense rotations [182,183] and accelerations [184,185], measure fundamental constants [184,186], monitor quantum decoherence [187] and characterize atomic and molecular properties [188].

Interferometers employing *trapped* cold neutral atoms [79, 82, 174, 189] form a separate category from the free-space atom interferometers. One of the several differences is the way beamsplitting is achieved. Instead of splitting in momentum space an atom cloud is split in position space by slowly transforming the trapping potential from single well to double well by ramping up a potential barrier. The phase can be read out either as population difference between the ground state and first excited state after recombination of the split cloud in the trap [190] or by releasing the clouds from the potential, overlapping them in expansion to generate an interference pattern [79]. For quantum degenerate gases the obtained pattern

is created by interference of the macroscopic wave function instead of single particle interference as in conventional atom interferometers. An advantage of the fact that the atoms are trapped is the possibility of long interrogation times promising more precise measurements, although there is discussion about the mechanism and timescale of decoherence which could be a limiting factor in this respect [191].

Although trapped cold atom interferometers do not necessarily have to be implemented on atom chips, these chips do have the potential advantage of being compact and even portable [192]. An additional advantage is that the splitting can be implemented purely magnetically, removing the need for additional lasers and further simplifying the instrument. Initially it was attempted to construct a atom-chip-based beamsplitter using purely magneto-static potentials produced by a multi-wire geometry [50, 190]. Shin *et al.* [155] used such a device to produce interference, but the phase of the interference was random. Technical difficulties like a weak confinement during the splitting and extreme sensitivity to magnetic field fluctuations prevented this design from being successful. The above technical problems can be avoided by using rf-dressed potentials to create the double-well, studied first experimentally by Schumm *et al.* [79]. This is currently the preferred technique for making atom-chip-based atom interferometers and is also the technique we use for the interference experiment which is the subject of this chapter.

6.2.2 The interference pattern

In order to obtain an expression for the interference pattern created by overlapping two independent condensates after releasing them from a double-well potential we follow Ref. [193]. We describe the two BECs with single-particle wave functions ψ_1 and ψ_2, each the solution of the Gross-Pitaevskii equation for its well. We assume each condensate has a well-defined initial phase. If there is coherence between the clouds, the state can be described as

$$\psi(\mathbf{r},t) = \sqrt{N_1}\psi_1(\mathbf{r},t) + \sqrt{N_2}\psi_2(\mathbf{r},t), \tag{6.2}$$

where the subscripts refer to condensate 1 and 2 and N is the expectation value of the number of particles in the cloud. After release of the condensates from the trap, they expand, overlap and interfere. Neglecting particle interactions between the two clouds, the particle density is given by

$$n(\mathbf{r},t) = |\psi(\mathbf{r},t)|^2 = N_1|\psi_1(\mathbf{r},t)|^2 + N_2|\psi_2(\mathbf{r},t)|^2 + 2\sqrt{N_1N_2}\mathrm{Re}\left[\psi_1(\mathbf{r},t)\psi_2^*(\mathbf{r},t)\right], \tag{6.3}$$

where Re denotes the real part. If the clouds are initially spherically symmetric Gaussian wave packets with radius R_0 separated by a vector $\mathbf{d}$ the wave functions are

$$\psi_{1,2}(\mathbf{r},t) = \frac{e^{i\phi_{1,2}}}{(\pi R_t^2)^{3/4}} \exp\left[-\frac{(\mathbf{r}\pm\mathbf{d}/2)^2(1+i\hbar t/MR_0^2)}{2R_t^2}\right], \tag{6.4}$$

where M is the atomic mass and ϕ_1 and ϕ_2 the initial phases of the two condensates, and the sign in front of $\mathbf{d}$ is different for the two clouds. For non-spherical

condensates scaling equations are available [194, 195]. The radius of the expanding wave function as a function of t is

$$R_t^2 = R_0^2 + \left(\frac{\hbar t}{M R_0}\right)^2 . \tag{6.5}$$

Substituting Eq. (6.4) in Eq. (6.3) yields

$$2\sqrt{N_1 N_2}\mathrm{Re}\left[\psi_1(\mathbf{r},t)\psi_2^*(\mathbf{r},t)\right] = c\cos\left(\frac{\hbar}{M}\frac{\mathbf{r}\cdot\mathbf{d}}{R_0^2 R_t^2}t + \phi_1 - \phi_2\right), \tag{6.6}$$

where c is an amplitude that slowly varies with spatial coordinates. The cosine term describes the interference pattern. From the argument of the cosine and for large expansion times such that $R_t^2 \gg R_0^2$, we see that the fringe spacing is equal to

$$\Delta z \simeq \frac{ht}{M|\mathbf{d}|}. \tag{6.7}$$

The lines of maximum intensity in the interference pattern are perpendicular to $\mathbf{d}$ and the exact position of the maxima depends on the phase difference between the clouds $\phi_1 - \phi_2$. The fringe spacing is equal to the de Broglie wavelength [Eq. (6.1)] of a particle with a velocity $|\mathbf{d}|/t$.

This treatment ignores the fact that an uncertainty relation exists between the particle numbers and the phase of a BEC [109, 193]. Despite this shortcoming we give this simple description here as it provides quick insight in the generation of the interference pattern. More advanced treatments employing phase states or number states that do obey the uncertainty relation (full quantum statistics), arrive at the very same result as Eq. (6.6) [109, 193].

6.2.3 The phase of the macroscopic wave function

Because the phase of the interference pattern is a measure for the phase difference between the two interfering condensates, it is only natural at this stage to look at a few of the most important properties of the phase of the macroscopic wave function describing a condensate. The condensate phase and long-range order have been the subject of many theoretical investigations. The ones most relevant here deal with the relation between long-range order and the dimensionality of the condensate [74, 113, 196–198].

The general picture is as follows. In three dimensions density fluctuations and phase fluctuations quickly vanish as a trapped Bose gas is cooled below T_c, the critical temperature for Bose-Einstein condensation. The fluctuations are suppressed by the mean-field interaction, yielding long-range order. In *elongated* three-dimensional ($k_\mathrm{B}T, \mu > \hbar\omega_\perp$) and one-dimensional ($k_\mathrm{B}T, \mu < \hbar\omega_\perp$) systems the situation is different. At finite temperature $T \ll T_c$ the density fluctuations are small, but along the length of the cloud phase fluctuations are present originating from thermal excitations. Such a phase fluctuating condensate is called a quasi-condensate. The characteristic length of the phase fluctuations is the phase coherence length:

$$L_\phi = \frac{\hbar^2 n_\mathrm{l}}{M k_\mathrm{B} T}, \tag{6.8}$$

where n_{l} is the longitudinal (linear) density. As the temperature is decreased the phase coherence length increases. T_ϕ is defined as the temperature for which the phase coherence length is equal to the condensate half length L such that the system crosses over to a true condensate, i.e.:

$$\frac{T}{T_\phi} = \frac{L}{L_\phi}, \tag{6.9}$$

and thus

$$T_\phi = \frac{\hbar^2 n_{\mathrm{l}}}{M k_{\mathrm{B}} L}. \tag{6.10}$$

Condensates in our setup are normally in the 3D to 1D cross-over ($\mu \sim \hbar\omega_\perp$) with a phase coherence length shorter than the length of the cloud ($T > T_\phi$). On slow transformation of the single-well potential to a double-well the cloud is split coherently meaning that the two resulting independent systems start with the same phase pattern as the initial gas. As soon as the gases are fully separated the phases will develop independently. After release from the trap the density decreases rapidly, switching off the interactions and freezing in the phase pattern. If the two condensates are released immediately after splitting, the phases have not had time to develop. Thus the phase difference is zero, independent on the position along the cloud and we expect straight interference fringes. If the condensates spend more time in the split potential the phase difference along the cloud can develop into a random pattern, resulting in a varying spatial phase of the interference pattern along the length of the cloud. As a consequence the fringes will appear wavy.

6.2.4 Properties of the double-well potential

Of practical importance in experiments employing a double-well potential for interferometric purposes as described here, are the exact splitting point, the double-well separation and the height of the barrier between the wells. The splitting frequency, or critical frequency ω_0, was found in Ch. 5 [Eq. (5.4)] to be

$$\omega_0 = \frac{|g_F \mu_B|}{\hbar}\left(B_I - \frac{b_{\mathrm{rf}}^2}{4B_I}\right), \tag{6.11}$$

where g_F is the Landé factor, μ_B the Bohr magneton, B_I the offset field in the longitudinal (x) direction and b_{rf} the strength of the rf-dressing field. At ω_0 the potential lacks harmonic confinement and is quartic in the splitting direction. For $\omega < \omega_0$ the potential has a single minimum, while for $\omega > \omega_0$ it is a double-well potential. The separation $|\mathbf{d}|$ between the two wells is [Eq. (5.6)]

$$|\mathbf{d}| = \frac{2}{q}\sqrt{B_0^2 - B_I^2}, \tag{6.12}$$

where q is the static magnetic field gradient above the chip and B_0, the strength of the static magnetic field in the potential minimum, is the positive solution to the quartic equation

$$B_0 - \frac{\hbar\omega}{|g_F \mu_B|} - \frac{b_{\mathrm{rf}}^2 B_I^2}{4B_0^3} = 0. \tag{6.13}$$

For small separation, such that $|\mathbf{d}| \ll B_I/q$, the magnetic field varies roughly quadratically with distance. Here we can approximate the separation with

$$|\mathbf{d}| = \frac{2\sqrt{2}}{q}\sqrt{\frac{\hbar B_I}{|g_F\mu_B|}}\sqrt{\omega-\omega_0}. \tag{6.14}$$

The potential barrier, U_b, is defined as zero for $\omega < \omega_0$. For frequencies $\omega_0 < \omega < \omega_L$ the minimum potential barrier is located in the middle between the two potential minima. We find to lowest order in $\omega - \omega_0$

$$U_\mathrm{b} \approx \frac{\tilde{m}\hbar^2\left(\omega-\omega_0\right)^2}{|g_F\mu_B|b_\mathrm{rf}}\left[\left(1+\frac{3}{4}\frac{b_\mathrm{rf}^2}{B_I^2}\right)\sqrt{1+\frac{b_\mathrm{rf}^2}{4B_I^2}}\right]^{-1}. \tag{6.15}$$

For our experimental parameters the term within the square brackets yields approximately 1. For $\omega > \omega_L$ the barrier height is no longer determined by the potential on the straight line connecting the two potential wells, but by the potential on the resonance circle in the y-z plane for a particular x. As a result the barrier increases more slowly for increasing rf frequency, and for $\omega \gg \omega_L$ approaches the asymptote $\tilde{m}|g_F\mu_B|b_\mathrm{rf}/2$ as

$$U_\mathrm{b} \approx \frac{\tilde{m}|g_F\mu_B|b_\mathrm{rf}}{2}\left(1-\frac{|g_F\mu_B|B_I}{\hbar\omega}\right). \tag{6.16}$$

6.3 Experimental optimization

6.3.1 General procedure

The experimental procedure for preparation of a BEC in the experiments described in this chapter is very similar to the procedure discussed in Ch. 5. In short, we produce a cold thermal cloud ($T \sim 1$ μK) containing 1.5×10^5 ^{87}Rb atoms in the $F = 2, m_F = 2$ state in the static magnetic trap (following the procedure detailed in Sec. 4.5). The magnetic field at the trap minimum is 2.86 G which corresponds to $\omega_L = 2\pi \times 2.00$ MHz. We switch on the rf-dressing field by ramping up the rf amplitude at a fixed frequency which is lower than ω_L, typically $0.99\,\omega_L$. At these settings the rf-dressed potential has a single minimum. We apply another weak rf field (~ 15 mG) to perform forced evaporative cooling in the dressed potential. The trap depth is reduced to approximately 1 μK over 350 ms by lowering the evaporation frequency. The resulting BEC contains 3×10^4 atoms. Next, the shape of the rf-dressed potential is changed by changing the frequency and/or the amplitude of the rf-dressing field. After a variable hold time in the final dressed potential, it is switched off. First the rf-dressing field is switched off by ramping down the rf amplitude to zero within 20 μs after which the static magnetic field is switched off by setting the currents through all wires and coils to zero.

Normally the entire switch-off procedure is fast with respect to the trap frequency to prevent the atoms from gaining momentum during switch-off. Because of the rapid switch-off we do not transfer all the atoms adiabatically from the $\tilde{m} = 2$ into

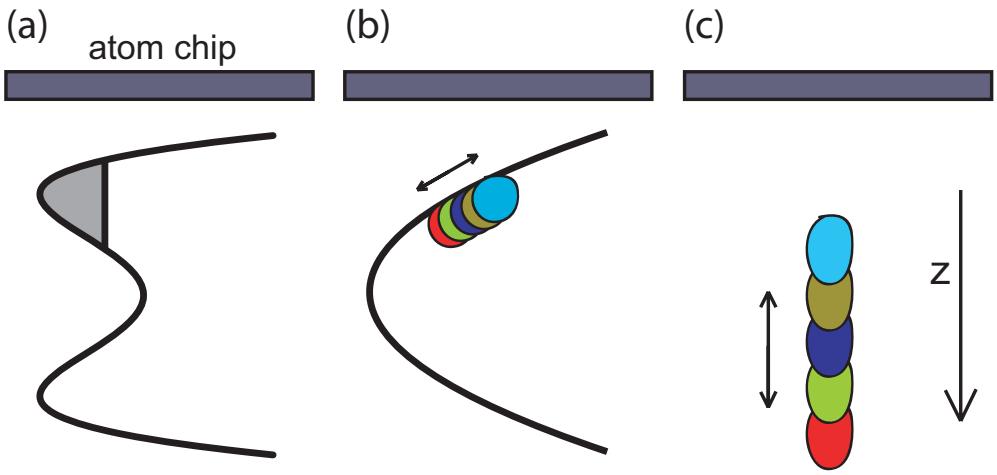

Figure 6.1: Cartoon illustrating the experimental procedure for switching off the double-well potential. A condensate is trapped in one of the potential minima of a vertically split double-well potential (a). After a certain hold time in this potential the rf-dressing field is switched off, creating a superposition of Zeeman states in the bare magnetic potential (b). The atoms start to accelerate in the magnetic potential — separating the spin components. Next the bare magnetic potential is also switched off allowing the atom cloud(s) to expand and accelerate under the influence of gravity (c).

the $m_F = 2$ state. Instead we typically obtain a distribution of the atoms over all available Zeeman states. This happens in all (atom-chip-based) experiments in which atoms are released from an rf-dressed potential [199], but is not necessarily a problem. It does cause trouble if small uncontrolled magnetic field gradients are present that accelerate the different Zeeman states differently, scrambling the spatial atomic distribution, leading to reduced observable fringe contrast. In the following two experiments we add a short ($\lesssim$ 2 ms) hold time in between switch-off of the rf and static field to completely separate each Zeeman component. After typically 15 ms of expansion we record a resonant absorption image with an illumination time of 80 μs. The switch-off procedure is shown schematically in Fig. 6.1.

6.3.2 Bare-trap dynamics after switch-off of the rf dressing

In this first experiment we use the Zeeman states that are created at switch-off of the rf-dressed potential to further characterize the underlying bare magnetic potential. This also yields unambiguous identification of the Zeeman components. The key ingredient in this experiment is a variable hold time in between the switch-off of the rf-dressing field and the static magnetic field. The difference in position of the minima of the two potentials gives the cloud a sizable amount of kinetic energy causing it to oscillate around the bare magnetic potential minimum. Two Zeeman states oscillate at their own frequency, one falls freely under gravity and two are accelerated to the chip surface making identification possible.

The precise experimental procedure deviates slightly from the general procedure

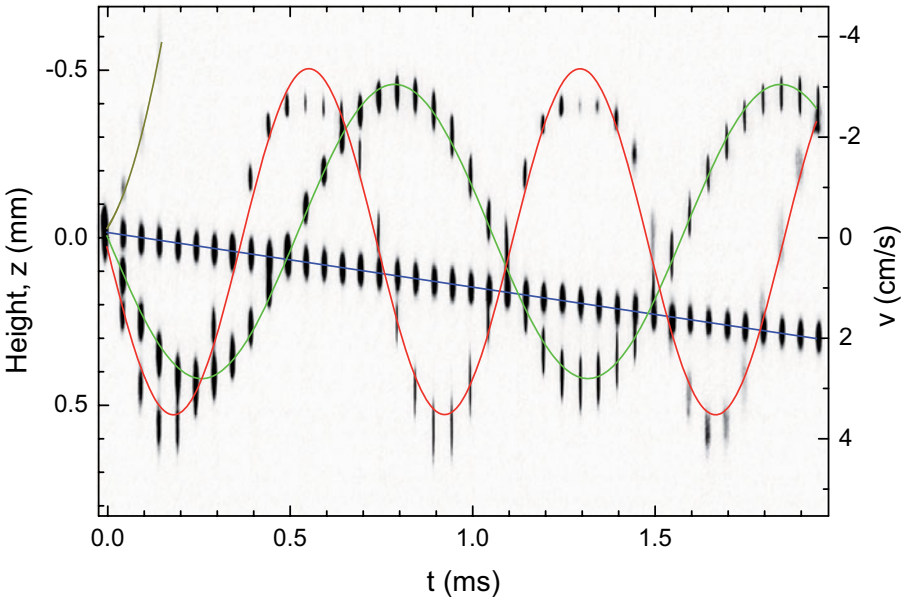

Figure 6.2: Oscillation of clouds of atoms in different Zeeman states in the bare magnetic trap after switch-off of the rf-dressed double-well potential. The atoms are imaged after 15 ms of ballistic expansion. The figure shows 40 images measured for a hold time of 0 to 2 ms. Each image is the average of ∼7 cycles of the experiment. The colored lines are fits to the data assuming harmonic confinement for $m_F = 2, 1$ and free fall for $m_F = 0$. The colors denote the different Zeeman states; red: $m_F = 2$, green: $m_F = 1$, blue: $m_F = 0$ and brown: $m_F = -1$.

described in Sec. 6.3.1. We switch on the rf-dressing field at 1.90 MHz and ramp it up to 2.05 MHz, vertically splitting the potential minimum before performing forced rf evaporation. A strong rf-dressing field gradient over-compensates gravity putting most atoms of the cold, but thermal, cloud in the upper of the two potential wells. Note that the Rabi frequency Ω is different for the potential wells due to the different distance to the field-producing wires. It is larger in the lower well, cf. Sec. 5.4.3. In the following stage of rf evaporation we sweep down the evaporation field frequency to 375 kHz. This is in between the two Rabi frequencies at the respective minima of the two wells, and efficiently removes all atoms from the lower potential well, while leaving a BEC in the upper well. The condensate contains $\sim 3 \times 10^4$ atoms. Switch-off of the rf-dressing field is done by ramping down the rf amplitude in 2.1 μs creating atoms in all Zeeman states. After a variable oscillation time t in that bare magnetic trap, we also switch that off. The atoms are imaged after 15 ms of time of flight.

The resulting absorption images as a function of oscillation time are shown in Fig. 6.2. Each image is the average result of 7 cycles of the experiment. Because of the relatively long time of flight, the measured relative position of the clouds is dominated by the velocity at switch-off. The relative position of the clouds after time of flight is plotted at the left-hand side, while the corresponding velocity immediately after release is indicated at the right of the figure. From fitting sine functions to the data (shown as red and green curves in the figure) we find oscillation frequencies

$\omega_\perp/2\pi$, of 1339 ± 6 and 942 ± 3 Hz. The fast oscillating cloud we identify as the $m_F = 2$ state, while the other is the $m_F = 1$ state. The ratio of the frequencies is $\sim\sqrt{2}$ confirming the factor 2 difference in magnetic energy of these two states. The $m_F = 0$ state accelerates under influence of gravity (blue curve). In 2 ms this cloud acquires a velocity of 2 cm/s. The $m_F = -1$ state is accelerated out of the trapping region in the first few images (brown curve).

The amplitude of the oscillation reflects the separation, d, of the two minima in the double-well potential as $d = 2v_0/\omega$ where v_0 is the maximum velocity. We find $d = 9.9$ μm and $d = 8.1$ μm for the $m_F = 1$ and the $m_F = 2$ clouds respectively. Both overestimate the calculated separation of the potential minima of 7.1 μm. Also notice that the oscillation centers of the two clouds do not match. A small magnetic field gradient at switch-off of the static magnetic potential may explain these observations.

As a final observation, we note that the shape of the different clouds in Fig. 6.2 changes with delay time t_0. The radial size (the vertical extension of the clouds) oscillates due to the change in radial confinement on going from the dressed to the bare potential. In the other, longitudinal direction we see the effect of condensate focusing. Condensate focusing is a technique in which a strong harmonic confinement is pulsed on briefly in order to transfer the momentum distribution of an elongated condensate to a spatial distribution allowing an direct, easy measurement of the momentum distribution [88,200,201]. In the experiment described here the longitudinal confinement is initially weak in the rf-dressed potential. In the following short hold time the atoms experience the bare potential with strong longitudinal confinement (50 Hz for $m_F = 2$) and are focused. By scanning the hold time in the bare trap the strength of the focus pulse is varied. For $\sim$0.8 ms the focus time matches the expansion time of 15 ms and we see a narrow atom distribution in Fig. 6.2. For the $m_F = 1$ state the focus pulse is weaker and it thus needs to stay on longer ($\sim$1.5 ms) to have the same effect.

This simple experiment in which we vary the trap time in the bare potential after switching off the rf dressing field provides information about the transverse and longitudinal confinement in the bare trap, the separation of the minima in the double-well potential and helps to identify the Zeeman states that are produced switching off the dressed potential.

6.3.3 Spin distribution

In this second experiment we study the influence of the rate at which we switch off the rf-dressed potential on the resulting spin state distribution. We aim to find a switch-off procedure which concentrates all atoms in one single Zeeman state, eliminating the complication of spatially separated atom distributions in time-of-flight.

For loading atoms in the dressed potential we use the general procedure described in Sec. 6.3.1. The rf-dressing field is switched on at 1.80 MHz. The rf amplitude, and thus also the rf gradient, we keep low ($\Omega \sim 2\pi \times 75$ kHz), such that gravity is not compensated [Eq. (5.9)], transferring the condensate completely to the lower

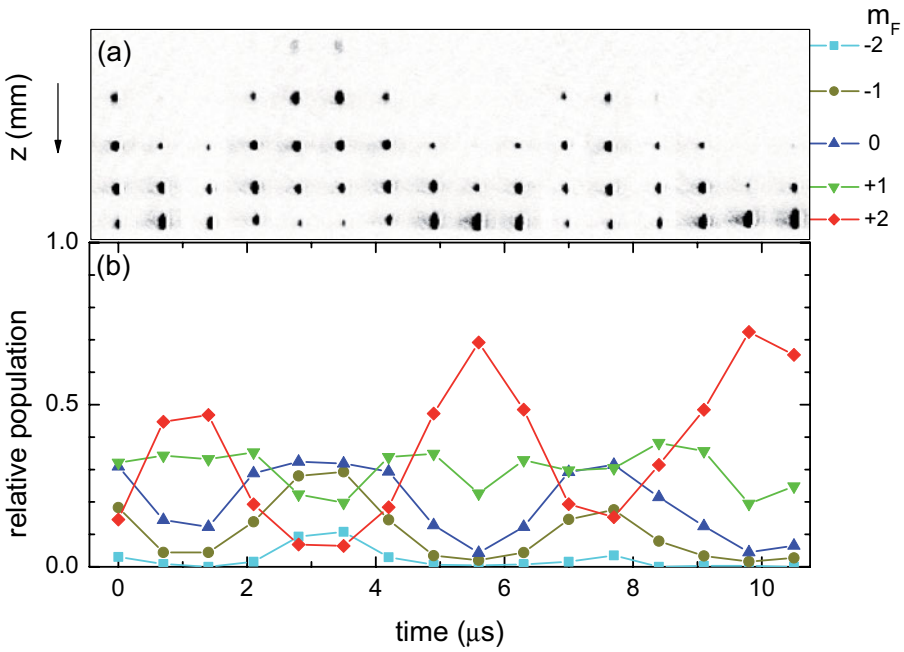

Figure 6.3: Population of spin states after release of a BEC trapped in one well of a double-well potential as a function of the rf-dressing field amplitude ramp down time. (a) Absorption images of the spatially separated spin states after 14 ms of expansion. The list of the states at the right (m_F=-2 (■), m_F=-1 (•), m_F=0 (▲), m_F=+1 (▼), m_F=+2 (♦)) shows the order of the states in (a). The population of the spin states in (b) was obtained from integration of the absorption images.

minimum of the vertically-split double-well potential. After reaching the final rf-dressing frequency of 2.02 MHz we increase the rf amplitude again to a more typical value ($\Omega \sim 2\pi \times 300$ kHz). Finally we release the atoms from the trap by ramping down the rf amplitude in a time t ($0 \leq t \leq 11$ μs). Simultaneously we decrease the rf-dressing frequency at a rate of 5 kHz/μs to shift the resonant surface away from the position of the atoms. After a hold time in the remaining bare magnetic potential of 0.2 ms to increase the spatial separation of the Zeeman states after time-of-flight, we also switch off the static magnetic trap.

The resulting distribution of the atoms over the Zeeman levels as a function of t is shown in Fig. 6.3. The absorption images in (a) show the spatial distribution of the atoms after 14 ms of time-of-flight. Each image is obtained from a single experimental cycle and thus has not been averaged. The 5 Zeeman states correspond to the 5 vertically separated clouds as indicated at the right-hand side of the figure. From integration of the absorption images we get the distribution of the atoms over the Zeeman states against rf-amplitude ramp-down time (b). It is observed to oscillate between a situation in which the atoms primarily occupy the $m = +2$ state and a one in which they are spread essentially over all available states.

To account for the observed Zeeman state distribution as a function of rf-amplitude ramp-down time we performed a numerical integration of the Schrödinger equation in the rotating frame [Eq. (A.9)]. The matrix elements $\tilde{H}_{km}$ are taken time-dependent as both the rf-dressing field amplitude and frequency vary in time. The

switch-off is fast with respect to the external movement of the atoms so to good approximation the atoms do not move through the static magnetic field during switch-off. In the calculation we keep the angular frequency of the rotating frame constant at the initial rf frequency throughout the integration. With this calculation we fail to reproduce the observed oscillatory behavior. Instead the population of the $m_F = 2$ state grows gradually over time until it saturates at 1 for switch-off times of 10 μs and longer. For the result it does not matter if we model the rf amplitude ramp down as a linear decrease over time or as a series of 0.7 μs steps, which is more realistic in view of the 0.7 μs programming time of the rf generators (see Sec. 4.4). The only way we can synthesize the oscillatory spin state population is by assuming initially a superposition of $\tilde{m} = 1$ and $\tilde{m} = 2$ in the double-well potential. A speculative explanation of the observed behavior is that such a superposition is created by an uncontrolled sudden variation in the potential at the start of the switch-off.

Although unable to account for the details of the observed behavior we can still optimize the experimental parameters to put as many atoms as possible in a single state. For the experimental conditions of Fig. 6.3 this would mean a ramp down time of 9.8 μs. We perform this optimization for each experiment as the optimum setting varies with rf dressing frequency and amplitude.

We conclude this section with a final remark on the phase of the rf-dressing field at switch-off. There are some concerns that the rf-dressing field phase has an influence on the Zeeman state distribution after release of the atoms from the trap [199]. We have performed a few experiments to investigate this. We varied the rf-dressing field phase while keeping all other parameters of the dressing field constant and not changing the rf-dressing field switch-off procedure. Under these conditions we did not observe any relation between the rf phase and the Zeeman state distribution.

6.4 Matter-wave interference

In a final experiment we succeeded in using the rf-dressed double-well potential to produce matter-wave interference. To realize an interference pattern that we can resolve optically (≥ 3 μm) we need a double-well potential with a separation relatively small (≤ 23 μm) compared to experiments previously described in this thesis and a BEC as pure as possible, equally divided over the two potential minima. The experimental procedure (Sec. 6.3.1) was optimized to achieve this.

The rf-dressing field is switched on at 1.95 MHz with $\Omega \approx 2\pi \times 300$ kHz to make a potential which is just below the splitting point ($\omega_0 = 2\pi \times 1.955$ MHz for these settings). After forced rf-evaporation in which a nearly pure BEC containing $\sim 3 \times 10^4$ atoms is produced, the rf-dressing frequency is ramped to 1.99 MHz to produce a double-well potential with a small separation calculated to be 5.8 μm. The rf evaporation field is left on after evaporative cooling to mitigate heating. As a result the atom number has dropped to $\sim 2 \times 10^4$ at the time of imaging. After a variable hold time the two clouds are released from the trap. The rf-dressing field amplitude ramp down time was set to 14.7 μs, optimized to put (nearly) all atoms

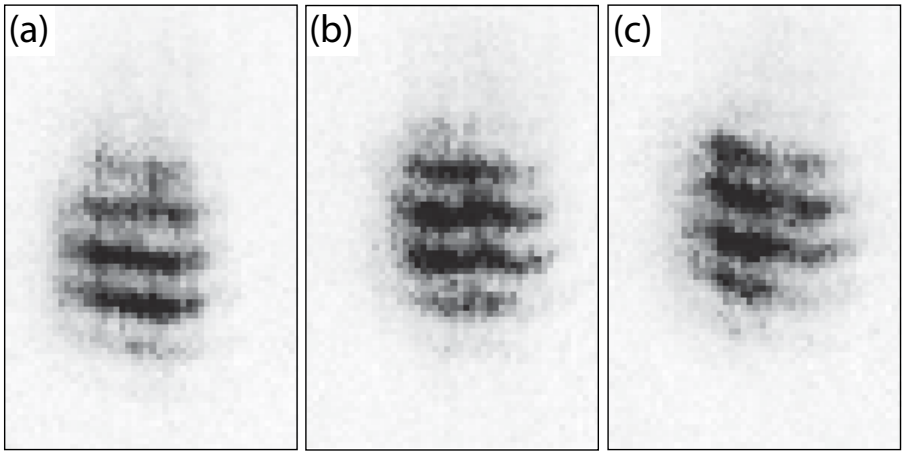

Figure 6.4: Absorption images of two BECs interfering after 15 ms of ballistic expansion following the release from the atom-chip-based rf-dressed double-well potential. Dimensions of each image are 108 μm $\times$ 161 μm. The hold time in the double-well potential is 6 ms and the final atom number $\sim 2 \times 10^4$. The three images were produced for identical experimental conditions.

in the $m_F = 2$ state after release (see Sec. 6.3.3). The release from the potential is fast with respect to all trap frequencies such that the atoms do not gain momentum during release. After 15 ms of ballistic expansion we perform absorption imaging of the overlapping clouds and observe the interference pattern.

To check whether the initial BEC is split completely we compare the chemical potential in the resulting double well to the height of the barrier separating the two final condensates. We obtain the chemical potential μ using the Thomas-Fermi approximation from numerical integration of the trapping potential

$$N = \iiint \frac{1}{g} \left(\mu - V(x, y, z)\right) \Theta(\mu - V) dxdydz, \tag{6.17}$$

where g is the 3D coupling constant as defined by Eq. (2.38) and $\Theta(x)$ the Heaviside step function. The chemical potential is $h \times 1300$ Hz and $h \times 1550$ Hz for a combined atom number in the two wells of 2×10^4 and 3×10^4, respectively. Both values are significantly less than the barrier height which is $h \times 4$ kHz [Eq. (6.15)], confirming the general picture described earlier in which the two clouds were treated as isolated condensates.

Three typical individual absorption images obtained under identical experimental conditions are shown in Fig. 6.4. We observe a matter-wave interference pattern containing 4 or 5 fringes. The fringes are not entirely straight indicating a development of the phase difference between the two condensates along the length of the two clouds during the period between splitting and release. From comparison of Fig. 6.4(a), (b) and (c) we see the exact pattern is different for each realization of the experiment.

To obtain more quantitative information information about the interference pattern we take a vertical slice integrated over a horizontal width of 10.75 μm (5 pixels)

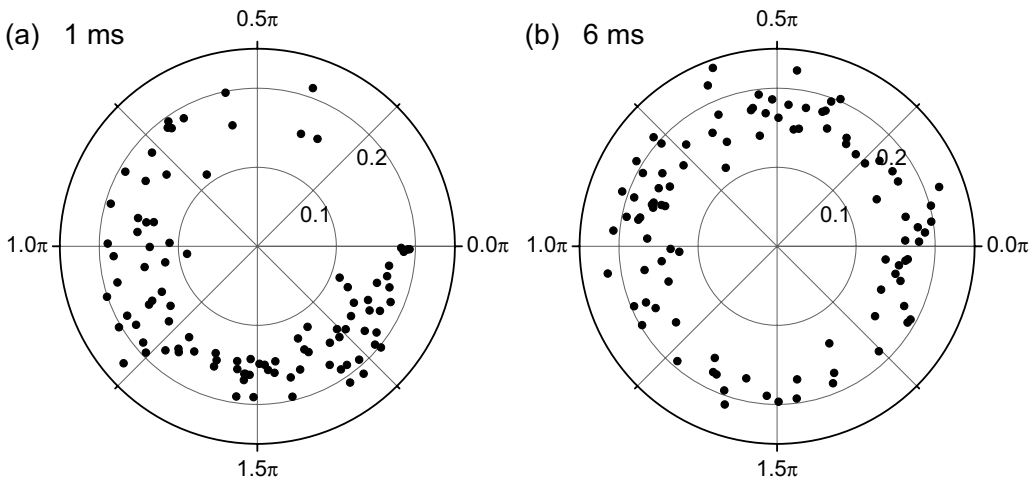

Figure 6.5: Phase distribution of the matter-wave interference pattern for ∼100 realizations of the experiment. The plotted phase is with respect to the Gaussian center of the cloud. The radius corresponds to the interference contrast (maximum 0.25). The data in (a) is for a hold time in the double well potential of 1 ms and has a mean phase of 4.6 rad, the width of the phase distribution is $\sigma = 1.4$ rad and the average interference contrast is 0.17 ± 0.03. The data in (b) are for a hold time of 6 ms and the values are 2.0 rad, 1.9 rad and 0.18 ± 0.02, respectively.

through the center of the cloud and fit the function

$$F(y) = A \exp\left[-\frac{(y-y_0)^2}{r^2}\right]\left[1 + C\cos\left(2\pi\frac{y-y_0}{\lambda} + \phi\right)\right], \tag{6.18}$$

where A is the overall amplitude, y_0 the cloud central position, C the interference contrast, λ the period of the interference pattern and ϕ the phase of the interference pattern with respect to y_0. The first, Gaussian, part of the function accounts for the overall shape of the cloud, while the cosine takes care of the interference pattern. After a time-of-flight of 15 ms the measured fringe period, $\lambda = 16.5$ μm, is 39% larger than the prediction of [Eq. (6.7)], $ht/md = 11.9$ μm. This is likely due to interactions and the exact shape of the potential. Schumm *et al.* have found a similar discrepancy in their experiments for small separations d [79, 202]. They compare the experimental data to the results of integration of the time-dependent Gross-Pitaevskii equation, along the lines of Ref. [203] and find much improved agreement compared to the above simple relation based on non-interacting clouds.

Because the phase information obtained from this fitting procedure has a circular nature, the usual ways to calculate average, standard deviation and variance do not suffice here. Instead we use definitions of these quantities that take into account the circular nature of the data [204]. This has already proven useful in matter-wave interference experiments [109]; we follow the same approach here. We transfer a set of measured phases ϕ_k to a unit circle

$$re^{i\overline{\phi}} = \frac{1}{N}\sum_{k=1}^{N} e^{i\phi_k}, \tag{6.19}$$

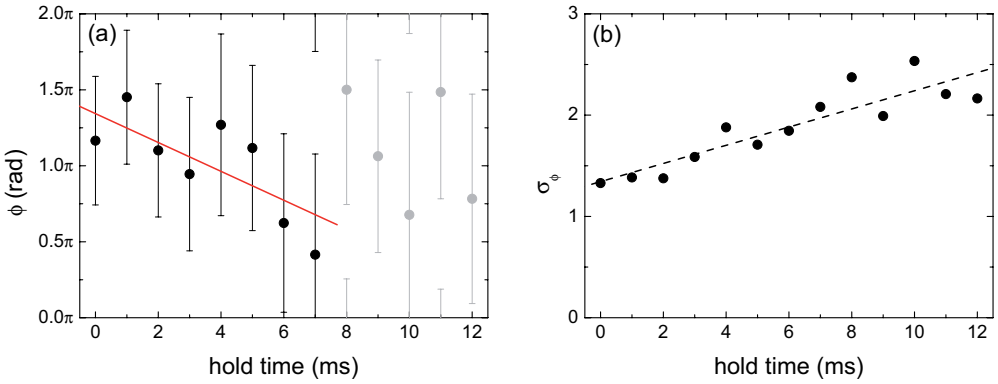

Figure 6.6: Development of the mean phase (a) and the circular standard deviation (b) against hold time in the double-well potential. The error bars in (a) also correspond to the circular standard deviation of the measured phases. The solid red curve is a linear fit to the data points for hold times up to 7 ms, having a slope of -0.34 rad/ms. For a hold time ≥ 8 ms σ becomes too large (see text for details), indicating a random distribution. In this case the mean phase does not carry any information. The dashed line (b) is a linear fit to the data points.

where N is the number of values, $\overline{\phi}$ the average phase and r the mean resultant length. This last quantity is a measure of the width of the distribution. It varies between 0 for a uniform distribution and 1 when all the phase values coincide. One can define the circular standard deviation [204], σ, as

$$\sigma = \sqrt{-2\ln(r)}. \tag{6.20}$$

For small σ ($\sigma \ll 2\pi$) the circular standard deviation is the same as that of the usual normal distribution. In this case it can be approximated by $\sigma = \sqrt{2(1-r)}$. For large σ it corresponds to the width of a normal distribution wrapped around the unit circle,

$$f(\phi) = \frac{1}{\sqrt{2\pi}\sigma} \sum_{k=-\infty}^{\infty} e^{-\frac{1}{2}\frac{(\phi-\overline{\phi}+2\pi k)^2}{\sigma^2}}. \tag{6.21}$$

The Rayleigh test [204] is used to distinguish between uniform and non-uniform distributions of circular data. An approximate form is given by

$$P = \exp\left[\sqrt{(1+4N+4N^2(1-r^2))} - (1+2N)\right], \tag{6.22}$$

where P is the probability that a uniform distributed data set produces a mean resultant length greater than r. Taking $N = 100$ and $P = 0.5$ shows that under these circumstances a distribution with a $\sigma \geq 2.2$ is most likely not to have a preferred direction.

The measured phase distribution for two different hold times is shown in Fig. 6.5. The phase is referred to the vertical center of the cloud removing the influence of shot-to-shot variations in the vertical cloud position after time-of-flight from the

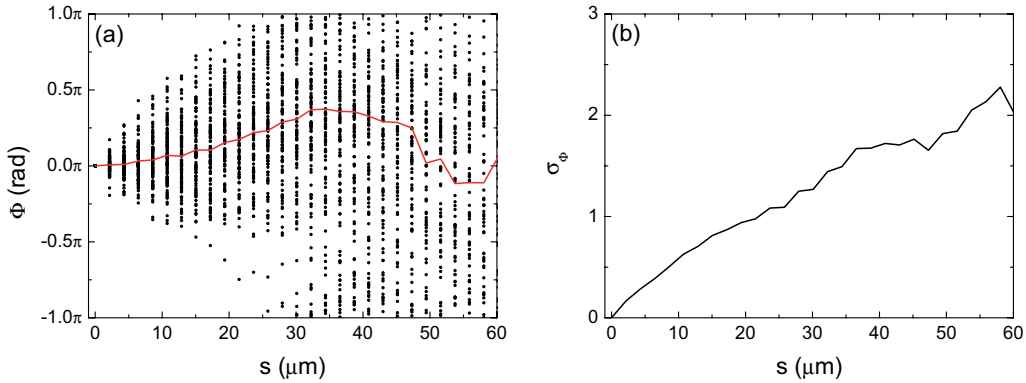

Figure 6.7: Distribution of the phase difference along the length of the cloud against the spatial distance s for ∼100 realizations of the interference experiment with a hold time of 6 ms in the double-well potential (a). The solid red curve is the mean phase difference. The curve in (b) shows the circular standard deviation of the distribution.

data*. We find a mean phase of 4.6 rad with $\sigma = 1.4$ (2.0 rad with $\sigma = 2.0$) for 1 ms (6 ms) hold time. From Eq. (6.22) with $\sigma = 1.4$ and $N = 98$ we find $P = 3.4 \times 10^{-7}$ while for $t = 6$ ms ($N = 97$) we find $P = 4.0 \times 10^{-2}$, indicating it is unlikely that either data set is associated with a uniform probability distribution.

The interference contrast is plotted as the radius in Fig. 6.5. The average is 0.18 ± 0.03 and approximately independent of hold time. The deviation of the interference contrast from 1 can be partially attributed to the resolution of the imaging system. For a fringe period of $\lambda = 16.5$ μm the maximum observable contrast is 60%.

Figure 6.6 shows the development of the mean phase and the circular standard deviation of the phase distribution against hold time. The increase of σ with hold time indicates a dephasing of the two condensates. As it becomes larger than 2.2 (hold time larger than 7 ms) the distribution can not be distinguished from a random distribution and the mean phase no longer carries any useful information. The solid curve in Fig. 6.6(a) is a linear fit to the plotted data points. The fact that we see a variation of the mean phase over time shows the phases of the two condensates are developing at different rates. The slope is -0.34 rad/ms corresponding to an energy difference of $h \times 54$ Hz possibly caused by an asymmetry in the trapping potential or a population imbalance of 9%. This is much smaller than the chemical potential and thus provides an excellent illustration of the sensitivity of atom interferometry.

To analyze the variation of the phase of the interference pattern along the length of the cloud we calculate $\Phi(s) = \phi(s/2) - \phi(-s/2)$, the phase difference between two points separated by a distance s, where these points are located at $x = -s/2$ and $x = +s/2$ with $x = 0$ the longitudinal center of the cloud. From one absorption image

*These variations in the cloud position are of the same magnitude of the period of the interference pattern. We attribute them to small, random fluctuations in the current of the magnetic field generating elements.

we obtain a series of Φ values for $s = 0$ to $s \leq 2L$, with L the condensate half length. By repeating the experiment we build up a full phase distribution distribution for each separation. The mean of this distribution is $\overline{\Phi}(s)$ and the circular standard deviation is $\sigma_\Phi(s)$, calculated from Eq. (6.19) and Eq. (6.20) respectively.

Figure 6.7 shows $\overline{\Phi}(s)$ and $\sigma_\Phi(s)$ extracted from the absorption images of ∼100 realizations for a hold time of 6 ms in the split trap. For this data $\phi(x)$ was obtained by integrating over a horizontal width of 4.3 μm (2 pixels) and fitting the function in Eq. (6.18), similar to the analysis for Fig. 6.5. In Fig. 6.7(a) all the data points and the corresponding average are shown as a function of s. The analysis presented here confirms the observations of Fig. 6.4 that the interference pattern is different for each experimental realization. The non-zero slope of mean phase difference with distance, shows that the interference fringes are, on average, not oriented perfectly horizontal, but have a preferred tilt. The curvature of the mean phase as a function of s indicates the fringes are not straight. The width of the phase distribution in Fig. 6.7(a) is shown in Fig. 6.7(b) by way of the circular standard deviation. We are now interested in the gradient of both the mean phase and of σ_Φ^2 for $s \to 0$. We assume the curvature near $s = 0$ is small enough for both quantities such that we can obtain the gradients by taking the slope of a linear curve fitted to the data points in the first 10 μm. The phase gradient $\frac{d\overline{\Phi}}{ds}$ is plotted in Fig. 6.8(a) against hold time. It is observed to vary between +0.3 rad/μm and -0.1 rad/μm. In our absorption images these phase gradients correspond to an average tilt of the interference fringes of +38° and -15°, respectively. The observed phase gradient corresponds to a relative momentum of the two BECs, with a maximum velocity of 220 μm/s. If we assume a harmonic oscillation with 25 Hz (the longitudinal trap frequency of the split trap) the amplitude is 1.4 μm, small compared to our optical resolution, and unobserved in the absorption images.

In order to extract a phase coherence length from our data it is useful to first recall the usual treatment for a single condensate. Petrov *et al.* [196] and Gerbier *et*

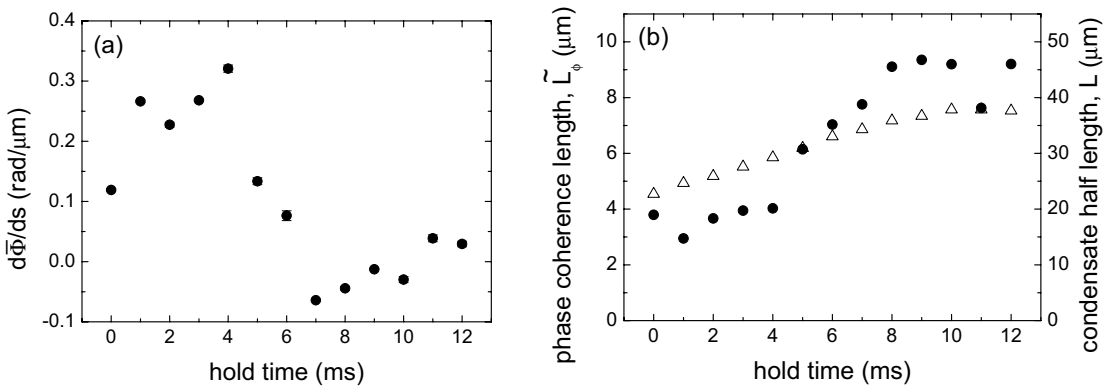

Figure 6.8: The relative phase gradient $d\overline{\Phi}/ds$ (a) and the phase coherence length $\tilde{L}_\phi$ [• in (b)] as a function of hold time in the split double-well potential. See the text for information on how these quantities are obtained. The condensate half length (L) [△ in (b)] is plotted for comparison.

al. [205] relate σ_Φ^2 of the phase difference between two points separated by a distance s to the phase coherence length. The relation

$$\sigma_\Phi^2(s) \approx \frac{T}{T_\phi}\frac{s}{L}, \tag{6.23}$$

connects the variance to a dimensionless temperature and a dimensionless separation. By substituting the characteristic phase-coherence length [Eq. (6.9)] one finds

$$L_\phi = \frac{s}{\sigma_\Phi^2}. \tag{6.24}$$

For the phase coherence length in our experiments we now use the notation $\tilde{L}_\phi$ to distinguish between the phase profile of a single condensate (L_ϕ) and the relative phase of two interfering clouds ($\tilde{L}_\phi$). We assume that the latter is similarly inversely proportional to the phase variance. We determine $\tilde{L}_\phi$ by taking the inverse of the slope of a linear curve fitted to the variance data for $0 \geq s \geq 15$ μm. The result is plotted in Fig. 6.8(b) as a function of hold time.

For perfect splitting, one would expect the phase patterns along the lengths of the split clouds to be identical, and $\tilde{L}_\phi$ to be infinite. This would then be followed by a gradual decrease to an equilibrium value as the phases develop independently [72]. We observe a different behavior. The phase coherence length *increases* for longer splitting times. We attribute this increase to the oscillation of the cloud length induced by the reduction of the longitudinal confinement of the double-well potential with respect to the potential in which the condensate was prepared.

6.5 Summary and outlook

In this chapter we have described results of initial experiments in which we interfere condensates released from a vertically split double-well rf-dressed potential and given information on the experimental optimization necessary to achieve these results. We have shown that upon switch-off of the rf-dressing field a distribution of Zeeman states is created, but by ramping down the rf amplitude in a controlled way in ~ 10 μs it is possible to put almost all atoms in the $F = 2, m_F = 2$ state. A great amount of information on the Zeeman state distribution and the trapping potential can be obtained from a simple experiment in which the trapping time in the bare potential after switch-off of the rf-dressing field is varied.

Releasing a split condensate from the double-well potential we observe interference fringes having an average contrast of 0.18. Detailed analysis of the phase of the interference pattern shows that splitting is at least partially coherent but the phase randomizes within 10 ms. Immediately after splitting we see a linear development of the mean phase indicating an energy difference between the two condensates of $h \times 54$ Hz. The observed interference fringes have a wavy appearance as one expects for elongated quasi-condensates. From analysis of the spatial fluctuations of the phase we find that the phase gradient varies in time between +0.3 rad/μm and -0.1 rad/μm which corresponds to a momentum of $\lesssim$220 μm/s or a dipole oscillation

amplitude of 1.4 μm. We also derive a phase coherence length which is typically 6 μm and grows *larger* possibly due to an oscillation of the condensate length. The oscillation is caused by a change in the longitudinal confinement when the transverse profile of the rf-dressed potential is changed. This effect was investigated in detail in Ch. 5 of this thesis.

Although the interference contrast is relatively low and there are signs the coherence is influenced by collective excitations of the condensate we still manage to extract useful information from the interference pattern. To improve on this in future experiments we intend to implement several changes: implementing longitudinal imaging and careful optimization to further enhance stability and reproducibility should prove useful. The analysis of the interference fringe pattern will be easier for longitudinal images as the fringes will be straight (not perturbed by longitudinal phase fluctuations). Also longitudinal images will allow one to see interference independent of the splitting direction of the double-well potential (including horizontal splitting to minimize the influence of gravity) as all directions are perpendicular to the imaging direction. By further careful optimization of the trapping and cooling sequence, collective excitations can be minimized. This should allow further interferometric studies of the intriguing coherence properties of (quasi)-one-dimensional degenerate Bose gases [72, 83].